Is the Water Vapor Supersaturation Distribution Gaussian?

SUBIN THOMAS,[a] PRASANTH PRABHAKARAN,[a] WILL CANTRELL,[a] AND RAYMOND A. SHAW[a]

[a] *Department of Physics, Michigan Technological University, Houghton, Michigan*

(Manuscript received 22 December 2020, in final form 27 April 2021)

ABSTRACT: Water vapor supersaturation in the atmosphere is produced in a variety of ways, including the lifting of a parcel or via isobaric mixing of parcels. However, irrespective of the mechanism of production, the water vapor supersaturation in the atmosphere has typically been modeled as a Gaussian distribution. In the current theoretical and numerical study, the nature of supersaturation produced by mixing processes is explored. The results from large-eddy simulation and a Gaussian mixing model reveal the distribution of supersaturations produced by mixing to be negatively skewed. Further, the causes of skewness are explored using the models. The correlation in forcing of temperature and water vapor fields is recognized as playing a key role.

KEYWORDS: Microscale processes/variability; Cloud microphysics; Large eddy simulations; Numerical analysis/modeling

1. Introduction

According to Köhler theory, cloud microphysical processes such as activation, deactivation, and growth of cloud particles depend on the mean thermodynamic properties of the environment surrounding the particle (Yau and Rogers 1996). These thermodynamic properties are determined by the temperature and water vapor content present in the system. Cloud particles respond to any nonequilibrium conditions present in the cloud system by condensational growth or evaporation according to the Le Chatelier's principle (Kostinski 2009). In a thermodynamically stable two-phase system, the water vapor pressure dynamically balances the condensation and evaporation fluxes over a flat, pure water surface at temperature T. This vapor pressure is called the saturation vapor pressure and is given by the Clausius–Clapeyron equation. Any excess/deficit of vapor pressure leads to nonequilibrium conditions, and is quantitatively expressed by supersaturation (s), and is given by

$$s = \frac{q_v}{q_{\mathrm{sat}}(T)} - 1. \tag{1}$$

Please refer to the appendix for variable definitions.

Cooper (1989) theoretically explored the implications of turbulent fluctuations on droplet size distributions, and recent experimental (Chandrakar et al. 2016; Prabhakaran et al. 2020; Chandrakar et al. 2020b), field (Gerber 1991; Ditas et al. 2012; Siebert and Shaw 2017; Yang et al. 2019), and numerical (Kulmala et al. 1997a,b; Vaillancourt et al. 2002; Paoli and Shariff 2009; Abade et al. 2018; Sardina et al. 2018; Li et al. 2018; Saito et al. 2019) studies have demonstrated the importance of scalar fluctuations caused by turbulence on activation, condensational growth and deactivation processes for aerosol and cloud particles, in addition to the mean supersaturation (Yau and Rogers 1996; Krueger 2020). Thus, an accurate representation of the supersaturation variability is required to capture the cloud microphysics effects (Hoffmann et al. 2019).

In modeling studies, if supersaturation is treated as a random variable at all, its probability density function (PDF) is usually treated as Gaussian (Sardina et al. 2018; Saito et al. 2019; Chandrakar et al. 2018), similar to scalars like temperature and water vapor mixing ratio. However, the supersaturation PDF is dependent on the process by which supersaturation is produced. In a parcel view of the atmospheric clouds, supersaturation can be produced by the vertical ascent of parcels (Yau and Rogers 1996) and by the isobaric mixing of parcels (Korolev and Mazin 2003). Cloud entrainment (Korolev and Isaac 2000; Pinsky and Khain 2018) and cloud-free Rayleigh–Bénard convection (Saito et al. 2019; Zhang et al. 2019; Chandrakar et al. 2020a) are examples of processes that can produce supersaturation via isobaric mixing, occurring both in nature and in the laboratory. For the current study, we focus on supersaturation generated via mixing processes and cloud-free Rayleigh–Bénard convection (RBC) is an ideal surrogate for such processes. RBC can be considered the simplest model of the subgrid-scale mixing within a typical cloud large-eddy simulation (LES), for example. It is further advantageous because it efficiently produces a statistically stationary thermodynamic state corresponding to the mixing processes. Furthermore, an atmospheric LES model can be modified to simulate cloud-free RBC to exclusively study mixing processes without any complexities and uncertainties involving cloud-supersaturation feedback interactions and boundary forcings. This model not only serves as the test bed to reveal insights into the nature of supersaturation PDF produced by mixing processes in the absence of cloud droplets, but also helps in validating a computationally inexpensive Gaussian mixing model introduced here.

In this study, we investigate the shape of the supersaturation PDF in the context of atmospheric mixing processes in the absence of cloud droplets using an atmospheric LES and a Gaussian mixing model detailed in section 3. The results are presented in section 4, and atmospheric implications are discussed further in section 5.

Corresponding author: Raymond A. Shaw, rashaw@mtu.edu

DOI: 10.1175/JAS-D-20-0388.1

2. Theory

a. Scalar equations

We begin by considering the origin of supersaturation fluctuations. The advection–diffusion equation of scalars with external large-scale forcing required to sustain the fluctuations is given by

$$\frac{\partial T}{\partial t} = \nabla \cdot (-\mathbf{U}T + \alpha \nabla T) + \frac{L_v}{C_p}\dot{q}_l + f_T, \tag{2}$$

$$\frac{\partial q_v}{\partial t} = \nabla \cdot (-\mathbf{U}q_v + \nu_v \nabla q_v) - \dot{q}_l + f_q. \tag{3}$$

Consider Eq. (2); the rate of change of temperature at a point depends on the temperature advected by the fluid motion, the diffusional heat transfer due to local gradients, rate of release/absorption of latent heat due to condensation/evaporation, and finally, any external forcing. Similarly in Eq. (3), for water vapor, all the terms on the right-hand side are analogous to Eq. (2) except for the latent heat effects term, which is replaced by rate of condensation/evaporation of water vapor. Note that we have used temperature (T) instead of pressure compensated potential temperature because isobaric mixing assumes the process to be local in nature. For parcel studies such as Abade et al. (2018), f_T and f_q represent the change in forcing of temperature and water vapor due to the entrainment of surrounding environmental air into the parcel.

From Eqs. (2) and (3) we gather that for a given flow field, the difference between appropriately normalized temperature and water vapor fields at a location can arise only from one of the following scenarios: (i) differential diffusivity of scalars, (ii) condensation/evaporation processes, and (iii) correlation between f_T and f_q.

In the absence of cloud droplets for a RBC system in steady state, the bulk mean temperature ($\overline{T}$) and water vapor ($\overline{q_v}$) are given by

$$\overline{T} = \frac{\rho_t T_t + \rho_b T_b}{\rho_t + \rho_b}, \tag{4}$$

$$\overline{q_v} = \frac{\rho_t q_{vt} + \rho_b q_{vb}}{\rho_t + \rho_b}. \tag{5}$$

In this context, *bulk* refers to the region of fluid sufficiently far away from the boundaries. Without considering the effects of turbulence, at a given pressure, the mean supersaturation expressed in mixing ratios is given by

$$\overline{s} = \frac{\overline{q_v}}{q_{\mathrm{sat}}(\overline{T})} - 1. \tag{6}$$

For a turbulent flow, Kulmala et al. (1997b) derived the supersaturation mean and variance to be Eqs. (7) and (8), respectively:

$$\overline{s} = \frac{\overline{q_v}}{q_{\mathrm{sat}}(\overline{T})}\left\{1 - \frac{L_v}{R_v \overline{T}}\frac{\overline{q_v' T'}}{\overline{q_v}\,\overline{T}} + \left[\frac{1}{2}\left(\frac{L_v}{R_v \overline{T}}\right)^2 \frac{\overline{T'^2}}{\overline{T}^2} + \frac{L_v}{R_v \overline{T}}\frac{\overline{T'^2}}{\overline{T}^2}\right]\right\} - 1, \tag{7}$$

$$\sigma_s^2 = \left(\frac{\overline{q_v}}{q_{\mathrm{sat}}(\overline{T})}\right)^2 \left\{\frac{\overline{q_v'^2}}{\overline{q_v}^2} - 2\frac{L_v}{R_v \overline{T}}\frac{\overline{q_v' T'}}{\overline{q_v}\,\overline{T}} + \left(\frac{L_v}{R_v \overline{T}}\right)^2 \frac{\overline{T'^2}}{\overline{T}^2}\right\}. \tag{8}$$

For random variables x and y, the ensemble mean is represented as $\overline{x}$, any fluctuations from the mean by prime x' and covariance terms by $\overline{x'y'}$.

To understand the role of turbulence on the mean supersaturation, one can subtract Eq. (6) from Eq. (7) and the role of turbulence is reflected by the difference. The coefficient of terms with $(T'/\overline{T})^2$ is always positive and hence tends to increase the mean supersaturation. On the other hand, the coefficient of the covariance term $\overline{q_v' T'}$ is negative; hence, its effect on mean supersaturation depends on the sign of the covariance term. In the subsequent subsection we explore the factors affecting $\overline{q_v' T'}$.

b. Discussions on the water vapor temperature covariance

On applying Reynolds decomposition for temperature and water vapor (e.g., refer to chapters 3 and 4 of Wyngaard 2010) by separating into mean and fluctuation components and subtracting the mean equations, we get the evolution equation for temperature and water vapor fluctuations:

$$\frac{\partial T'}{\partial t} = \nabla \cdot (-\overline{\mathbf{U}}T' - \mathbf{U}'\overline{T} + \alpha \nabla T' - \overline{\mathbf{U}'T'}) + \frac{L_v}{C_p}\dot{q}_l' + f_T, \tag{9}$$

$$\frac{\partial q_v'}{\partial t} = \nabla \cdot (-\overline{\mathbf{U}}q_v' - \mathbf{U}'\overline{q_v} + \nu_v \nabla q_v' - \overline{\mathbf{U}'q_v'}) - \dot{q}_l' + f_q. \tag{10}$$

To derive the evolution equation for $\overline{q_v' T'}$, we multiply Eq. (9) with q_v' and Eq. (10) with T':

$$q_v'\frac{\partial T'}{\partial t} = q_v'\nabla \cdot (-\overline{\mathbf{U}}T' - \mathbf{U}'\overline{T} + \alpha \nabla T' - \overline{\mathbf{U}'T'}) + \frac{L_v}{C_p}q_v'\dot{q}_l' + q_v' f_T, \tag{11}$$

$$T'\frac{\partial q_v'}{\partial t} = T'\nabla \cdot (-\overline{\mathbf{U}}q_v' - \mathbf{U}'\overline{q_v} + \nu_v \nabla q_v' - \overline{\mathbf{U}'q_v'}) - T'\dot{q}_l' + T' f_q. \tag{12}$$

Summing Eqs. (11) and (12) we obtain

$$\begin{aligned}\frac{\partial q_v' T'}{\partial t} = {} & -q_v'\nabla \cdot (-\overline{\mathbf{U}}T' - \mathbf{U}'\overline{T} + \alpha \nabla T' - \overline{\mathbf{U}'T'}) \\ & - T'\nabla \cdot (-\overline{\mathbf{U}}q_v' - \mathbf{U}'\overline{q_v} + \nu_v \nabla q_v' - \overline{\mathbf{U}'q_v'}) \\ & + \frac{L_v}{C_p}q_v'\dot{q}_l' - T'\dot{q}_l' + q_v' f_T + T' f_q.\end{aligned} \tag{13}$$

The time evolution of $\overline{q_v' T'}$ is obtained by averaging Eq. (13):

$$\begin{aligned}&\frac{\partial \overline{q_v' T'}}{\partial t} + \overline{\mathbf{U}} \cdot \nabla(\overline{q_v' T'}) + \overline{\mathbf{U}'} \cdot \nabla(\overline{q_v' T'}) + \overline{\mathbf{U}'T'} \cdot \nabla(\overline{q_v}) + \overline{\mathbf{U}'q_v'} \cdot \nabla(\overline{T}) \\ &= \nu_v \nabla^2(\overline{q_v' T'}) - \nu_v 2(\overline{\nabla q_v' \nabla T'}) + (\mathrm{Le} - 1)\nu_v \overline{q_v' \nabla^2 T} \\ &\quad + \frac{L_v}{C_p}\overline{\dot{q}_l' q_v'} - \overline{\dot{q}_l' T'} + \overline{T' f_q} + \overline{q_v' f_T}.\end{aligned} \tag{14}$$

In Eq. (14), the first term on the left-hand side is the time evolution of $\overline{q_v' T'}$, while the second and the third terms

represent advective transport by mean and fluctuating components of the flow. The fourth and fifth terms on the left-hand side are the two sources for production of $\overline{q_v' T'}$ due to the presence of a mean gradient in temperature and water vapor. The interpretation of the right-hand side of Eq. (14) is complicated due to the production of local gradients in temperature and water vapor due to phase change processes.

For the ease of interpretation, let us assume a case in the absence of droplets and external forcing. Therefore, terms with $\dot{q}_l'$ disappear from the right-hand side of Eq. (14) and only the diffusive terms are retained. For such a case the right-hand side can be rewritten as

$$\nu_v \nabla^2(\overline{q_v' T'}) - \nu_v 2(\overline{\nabla q_v' \nabla T'}) + (\mathrm{Le} - 1)\nu_v \overline{q_v' \nabla^2 T}, \tag{15}$$

where $\mathrm{Le} = \alpha/\nu_v$ is the Lewis number. These terms on the right-hand side of Eq. (15) can be interpreted as follows: the first term is the diffusive transport of $\overline{q_v' T'}$ and the second term is the dissipation term since $\overline{\nabla q_v' \nabla T'}$ is positive definite since both scalars behave identically in the flow field. The third term is relevant for cases with differential diffusivity, $\mathrm{Le} \neq 1$. The effects of differential diffusivity make the interpretation of the term difficult without a fully resolved study. It should be noted that these effects are significant only at diffusive length scales.

To evaluate the phase change effects, consider a system with temperature and water vapor transported only by advection processes but including condensation effects. In such a case, any local condensation results in the depletion of water vapor and increase in temperature and vice versa for any local evaporation. Therefore, $(L_v/C_p)\overline{\dot{q}_l' q_v'} - \overline{\dot{q}_l' T'}$ would always be negative and hence acts as a sink term for $\overline{q_v' T'}$. However, in physical systems phase change events produce local gradients of temperature and water vapor, resulting in interactions of all terms on the right-hand side of Eq. (14). Strictly speaking, these processes can only be disentangled through particle-resolved simulations of the turbulent flow, i.e., even beyond direct numerical simulation of turbulence, down to the temperature and vapor gradients existing at particle scales. Here, we will focus primarily on the supersaturation PDF without cloud droplet growth.

The production terms $\overline{\mathbf{U}' T'} \cdot \nabla \overline{q_v}$ and $\overline{\mathbf{U}' q_v'} \cdot \nabla \overline{T}$ in Eq. (14) are active only close to the boundaries where $\nabla \overline{T}$ and $\nabla \overline{q_v}$ are significant. The terms $\overline{\mathbf{U}' T'}$ and $\overline{\mathbf{U}' q_v'}$ at these boundaries are generally modeled using Monin–Obukhov similarity theory. The diffusive terms in atmospheric models are modeled using subgrid-scale parameterizations. Finally, the rate of condensation depends on the microphysical parameterization. It should be noted that the time rate of change of $\overline{q_v' T'}$ depends entirely on the level of approximation with reality by Monin–Obukhov similarity theory, subgrid-scale parameterization of diffusivity and microphysics.

3. Analysis tools

In this paper, we use two computational approaches to explore supersaturation fluctuations in a turbulent Rayleigh–Bénard convection flow. First, we describe a detailed large-eddy simulation approach, and second, we introduce an idealized Gaussian mixing model based on observed behavior of scalar fields from measurements and numerical studies of Rayleigh–Bénard convection. The latter model also can explore the effect of differential diffusivity, forcings of temperature and water vapor and their correlations on the supersaturation PDF.

a. LES

The System for Atmospheric Modeling (SAM) (Khairoutdinov and Randall 2003) coupled with Hebrew University Spectral Bin Microphysics (Khain et al. 2000; Fan et al. 2009) is configured to simulate the Michigan Tech Pi Cloud Chamber as described in Thomas et al. (2019). We provide a brief discussion of the model for completeness. The RBC system is a 2 m × 2 m × 1 m box modeled as 64 × 64 × 32 grid points with a grid size of 3.125 cm. The convective system is initialized by imposing an unstable temperature gradient and water vapor mixing ratio gradient along the height of the chamber, keeping the top and bottom boundaries saturated. Furthermore, adiabatic conditions for temperature and water vapor mixing ratio are imposed for the sidewalls. Once initialized, the system is allowed to evolve for 2 hours of physical time and the simulation reaches a stationary state in 20 minutes. The results from the last 1 hour of the simulation are used for the analysis presented here.

b. Gaussian mixing model

The isobaric mixing process in a turbulent cloud-free RBC system is emulated using a Gaussian mixing model. In the model, the PDFs of temperature and water vapor are assumed to be Gaussian in nature, as is observed for the bulk fluid in turbulent RBC (Niemela et al. 2000; Sreenivasan 2019; and references therein). The mean for temperature and water vapor are given by Eqs. (4) and (5). The standard deviation required for the description of a Gaussian PDF in RBC is given by Eqs. (3.6) and (3.7) from Chandrakar et al. (2020a) and can be rewritten as

$$\sigma_T^* = C^{-1/2} \mathrm{Ra}_m^{-1/6} \left(\frac{z}{H}\right)^{-1/2}, \tag{16}$$

$$\sigma_{q_v}^* = C^{-1/2} \mathrm{Ra}_m^{-1/6} \mathrm{Sc}^{-1/2} \mathrm{Pr}^{1/2} \left(\frac{z}{H}\right)^{-1/2}, \tag{17}$$

with

$$\sigma_T^* \equiv \sigma_T \Delta T^{-1},$$

$$\sigma_{q_v}^* \equiv \sigma_{q_v} \Delta q_v^{-1},$$

$$C = \kappa\, C_1^{-2}.$$

Here, Ra_m is the ratio of time scale for transportation via diffusion to convection, Pr is the ratio of momentum diffusivity to thermal diffusivity, Sc is the ratio of momentum to vapor diffusivity, and Le is the ratio of thermal diffusivity to vapor diffusivity or Sc/Pr. The procedure for calculating C is described next. For a given temperature difference, the mean and standard deviation of temperature are obtained at the midplane ($z = H/2$) of the RBC cell using LES. From Eqs. (16) and (17), C is calculated after setting Pr equal to Sc since the effects of differential diffusivity are not captured in the current LES

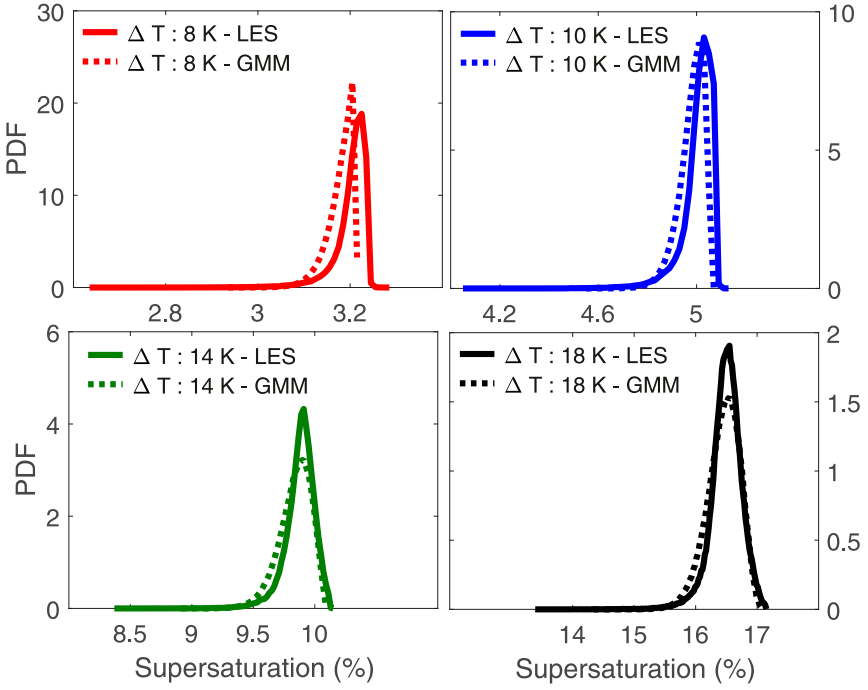

FIG. 1. Cloud-free Rayleigh–Bénard convection supersaturation PDFs for different temperature differences (ΔT, refer to labels) centered at the same mean temperature (T_m = 283.16 K). As the temperature difference increases, the supersaturation PDF becomes more symmetric. The LES data are obtained from the *bulk*, whereas the GMM data are obtained at the center of the chamber $z = 0.5H$.

model. The mean value of C is 3.378 and its standard deviation is 0.51 from the 4 LESs. In the absence of any trend, for the subsequent calculations, C is assumed to be a constant 3.378. A Gaussian profile is assumed for the temperature and water vapor, with the mean values calculated using Eqs. (4) and (5). Thus, a single realization of random variables—temperature and water vapor mixing ratio—is obtained by the following expression:

$$T = \overline{T} + \sigma_T \mathcal{N}_T(0,1), \tag{18}$$

$$q_v = \overline{q_v} + \sigma_{q_v} \mathcal{N}_{q_v}(0,1). \tag{19}$$

Here, $\mathcal{N}_T(0, 1)$ and $\mathcal{N}_{q_v}(0, 1)$ are normally distributed Gaussian random numbers with zero mean and unit variance. Generally, $\mathcal{N}_T$ and $\mathcal{N}_{q_v}$ need not be correlated; however, for physical systems one can expect a certain level of correlation between the temperature and water vapor scalars. From LES results, we find this correlation coefficient to be 0.9994. We use Cholesky decomposition of the T–q_v covariance matrix to generate a lower triangular matrix and its transpose, and further we use the resulting lower triangular matrix to create any desired correlation coefficient between the temperature and water vapor scalars.

Figure 1 shows the supersaturation PDFs of four cases with temperature differences of 8, 10, 14, and 18 K. The solid line shows the data obtained from LES at the midplane of the chamber, at least 12.5 cm away from the sidewalls. The dashed lines are the results from the Gaussian mixing model (GMM) with correlation coefficient between T and q_v to be 0.9994 and the constant C set to 3.378. We notice the shapes of the PDFs are qualitatively the same and the modes are shifted by 10% maximum. This level of agreement of the GMM will suffice for exploring the qualitative behavior of the supersaturation distribution under varying assumed T–q_v correlations.

Assuming the correlation coefficient between temperature and water vapor remains the same, the effects of differential diffusivity of scalars are explored by varying Pr and Sc. To understand the effect of scalar forcings, the correlation coefficient between $\mathcal{N}_T(0, 1)$ and $\mathcal{N}_{q_v}(0, 1)$ is changed and further in section 4 explored without considering the differential diffusivity effects.

4. Results

The supersaturation PDFs simulated using LES are shown in Fig. 1, for temperature differences of 8, 10, 14, and 18 K with an initial mean of 283.16 K. Though the bulk temperature and bulk water vapor PDFs are Gaussian in nature, a negatively skewed supersaturation PDF is observed in the bulk of the chamber. From Table 1, it is clear that the magnitude of the skewness is larger at lower temperature differences than at higher values. For LES, the term "bulk" here refers to all the grid cells that are at least 12.5 cm away from the walls of the chamber, in order to avoid the wall effects.

TABLE 1. Mean, mode, and skewness of supersaturation for different temperature differences. These results are obtained from the LES starting with a mean temperature of 283.16 K. Note the decrease in supersaturation skewness as ΔT increases.

ΔT (K)	$\overline{T}$ (K)	σ_T (K)	Mean (%)	Mode (%)	Skewness
8	283.09	0.2492	3.201	3.22	−2.70
10	283.05	0.3993	4.985	5.04	−2.47
14	282.94	0.5012	9.842	9.91	−1.51
18	282.86	0.6041	16.437	16.53	−1.14

To understand this negative skewness, the supersaturations obtained from the LES runs are plotted against temperature. A mixing curve obtained by mixing parcels from top and bottom plates, characterized by different temperature and saturated water vapor mixing ratios, in different proportions, is also shown. In Fig. 2 the mixing curves (dashed lines) are plotted in supersaturation and temperature coordinates. The filled circles are the LES results from the bulk of the chamber. For a RBC system without the density effects, the density-weighted mean temperature is the mean temperature between the top and the bottom plates. At low temperature differences, the peak of the mixing curve coincides with the density-weighted mean temperature; hence, the mode of supersaturation is the maximum supersaturation. As the temperature difference increases, the peak of the mixing curve shifts to lower temperature. This leftward shift of the mixing curve arises from the nonlinear nature of the Clausius–Clapeyron equation. Hence, the density-weighted mean temperature in the fluid moves from the maximum to the relatively linear region of the mixing curve. Furthermore, the region of the mixing curve sampled by the *bulk* increases, due to the increased variance of temperature and water vapor as a result of increase in Rayleigh number. Though density effects (non-Boussinesq effects) can counteract these effects by reducing the positive skewness of the mixing curve and reducing the mean temperature, these effects are negligible for our conditions (refer to Table 1). Please note that all of the mixing line is not populated because only the bulk is sampled, the rest of the mixing line can be sampled from the boundary layer regions near the top and bottom walls.

Figure 3a plots q_v versus T, comparing the Gaussian mixing model (red dotted line) and LES results (blue). Notice that they lie on a straight line joining the points corresponding to the state of the top and bottom plates. Figure 3b compares the supersaturation PDFs obtained from the LES and the GMM. The deviation of the model from the LES results is probably due to the approximation of scalar fluctuations to be Gaussian. The skewness of the temperature data from the LES reveals a slight positive skewness on the order of 0.1, compared to 0.0 for a perfect Gaussian distribution. The NOB effects drive the mean *bulk* temperature to slightly less than the average of top and bottom plate temperatures; hence, more positive fluctuations arise to reduce this difference.

Figure 4a illustrates the effect of differential diffusivities on supersaturation fluctuations. The case $\nu_v = \alpha = \mathrm{Le}^{-1} = 1$, shown in red is the diffusivity formulation ubiquitous across

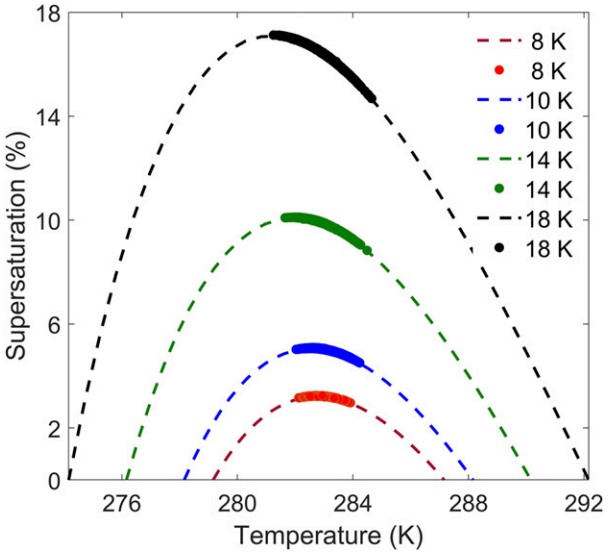

FIG. 2. Supersaturation vs temperature, illustrating the mixing line (dashed line) and LES data (filled circles) for different temperature differences (ΔT, refer to labels) centered at the same mean temperature ($T_m = 283.16$ K). Note that only a small part of the mixing curve is sampled during a turbulent mixing process in the bulk. The part of the mixing curve sampled becomes less symmetric as the temperature difference is increased.

LES and most DNS. As discussed earlier, this result in a negatively skewed distribution of the supersaturation PDF. The physical diffusivities follow $\mathrm{Le}^{-1} = 1.16$, and the role of differential diffusivity is explored with Le^{-1} of 0.75 and 1.33. An interesting observation is that except for when $\mathrm{Le}^{-1} = 1$, the mixing process no longer follows an isobaric mixing line (black dotted line). From the earlier arguments based on the density-weighted mean temperature, it is easy to see that the differential diffusivities do reduce the negative skewness of supersaturation as illustrated in Fig. 4b. However, note that the PDF is still non-Gaussian and negatively skewed with $\mathrm{Le}^{-1} = 1.16$. A detailed treatment of differential diffusivity and its role in the supersaturation PDF pertaining to RBC can be found in Chandrakar et al. (2020a).

In all the cases discussed above, the forcings of temperature and water vapor, f_T and f_q, respectively, have a perfect correlation. In Fig. 5a we can see a broad symmetric supersaturation PDF for uncorrelated and anticorrelated forcings of temperature and water vapor. We recall that for a cloud-free RBC system, as described in section 3, the minimum saturation ratio that is allowed is 100%. However, for lower correlation coefficients, saturation ratios are as low as 90% as show in the figure. Any decrease in forcing correlation from a perfect correlation coefficient of 1 (shown in blue) results in a change in the average slope of the distribution of points (Fig. 5a) and an increased spread of the distribution of points around the average slope. From Fig. 5b, it is observed that the spread reaches a maximum when the scalar forcings are perfectly uncorrelated (shown in red) and as they become anticorrelated the spread starts to reduce and falls on a line for correlation coefficient of −1 (shown in green). During this process, the

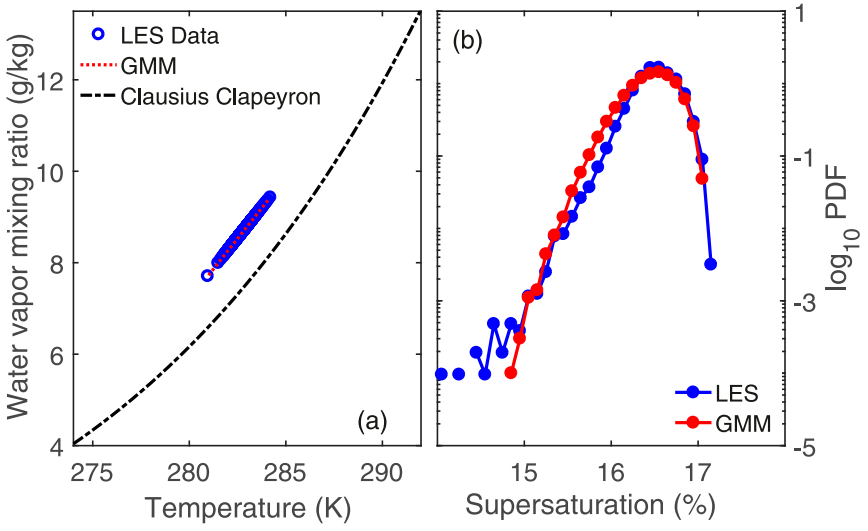

FIG. 3. (a) Water vapor mixing ratio vs temperature, showing the Clausius–Clapeyron line (black dashed line), LES data (blue filled circles), and GMM data (red dotted line). (b) Comparison of supersaturation PDF of LES data (blue) and GMM data (red); notice LES data have a longer negatively skewed tail compared to GMM results. Plots are generated with $\Delta T = 18$ K and $T_m = 283.16$ K. LES assumes the same turbulent diffusivities for temperature and water vapor, and for comparison the GMM also assumes the same diffusivities for temperature and water vapor in the calculation of standard deviations of these scalars.

points fall below the limit imposed by the Clausius–Clapeyron line resulting in subsaturated conditions.

Figure 6 illustrates the effect of cloud droplet growth on the supersaturation generated by mixing. The blue dots represent the mixing line in the absence of cloud droplets and red dots represent the mixing in the presence of cloud droplets at the high Damköhler (Da) number limit (Chandrakar et al. 2016). The high Da case is similar to the bulk microphysics limit for which the mixing leads to points collapsing onto the Clausius–Clapeyron line. In Fig. 6 the straight, cloud-free mixing line approaches the Clausius–Clapeyron curve as the Damköhler number increases. The slight deviation the from Clausius–Clapeyron curve can either be the result of a numerical artifact or a physical process and cannot be resolved using the current LES model. This transition requires careful investigation and will be explored in a future study.

5. Discussion and concluding remarks

The comparison and verification of the previously demonstrated numerical results with experiments is the focus of ongoing research. It depends on making measurements of the distribution of supersaturation in a turbulent flow, which is a significant experimental challenge. Very few direct measurements are available from the field (Gerber 1991; Siebert and Shaw 2017). Progress toward in situ measurement of supersaturation in cloud-free Rayleigh–Bénard convection is discussed in Anderson et al. (2021, manuscript submitted to *Atmos. Meas. Tech. Discuss.*). Efforts for simultaneous remote measurement of temperature and water vapor concentration at sufficiently high precision for obtaining reliable supersaturation estimates are also being made (Capek et al. 2020).

In the current study, we use LES and a Gaussian mixing model to explore the isobaric mixing processes in an idealized turbulent cloud-free Rayleigh–Bénard convection system. In the idealized system we observe the supersaturation PDF to be non-Gaussian and negatively skewed, as shown in Fig. 1. Further, we observe the PDF to be more negatively skewed for smaller temperature differences than at higher temperature differences.

To understand the supersaturation PDF and how it may be generalized to other contexts, we explore the covariance term $\overline{q_v' T'}$. We identify differential diffusivity, condensation/evaporation processes and the correlation coefficient between any forcing of temperature and water vapor as possible causes of any change in the magnitude of the covariance $\overline{q_v' T'}$. For example, using the GMM we notice that the supersaturation PDF tends to be less skewed when differential diffusivity is accounted for.

A detailed understanding of the effect of condensation/evaporation on $\overline{q_v' T'}$ would require a dedicated study over a range of microphysical conditions. However, for a high Dämkohler number (Chandrakar et al. 2016) case, we observe that the mixing line falls on the Clausius–Clapeyron curve, assuming the same diffusivity for temperature and water vapor. In Hoffmann et al. (2019) it is observed that the supersaturation PDF tends to become narrower in the interior of the cloud, consistent with the high Dämkohler number predictions from Chandrakar et al. (2016). Such a narrowing of the supersaturation PDF can be observed in the current study also—however, the detailed source of destruction of the width of the supersaturation PDF would require a cloud droplet resolved study.

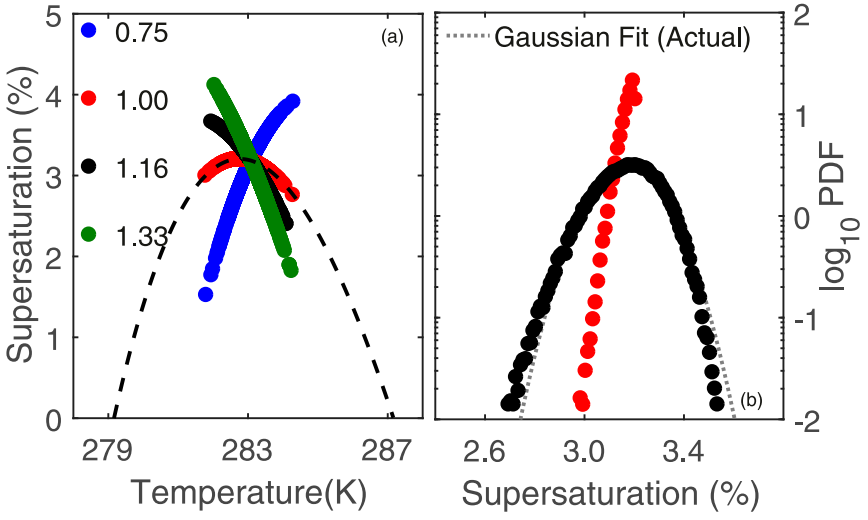

FIG. 4. Supersaturation vs temperature and supersaturation PDFs illustrating the effect of differential diffusivity in the mixing process, by varying the ratio of ν_v/α shown in different colors. (a) The distribution of these points about the mixing curve (dashed black curve). (b) PDF generated with real physical diffusivities (black) compared to a case with same diffusivities (red). The differential diffusivity results in a deviation from theoretical mixing processes and this deviation results in the reduction of negative skewness. Though differential diffusivity reduces the skewness of the supersaturation PDF and increases the left–right symmetry, the supersaturation PDF is still negatively skewed. Results are obtained from the GMM for $\Delta T = 8$ K.

A key point emerging out of the current study is the importance of correlation coefficient between external forcings of temperature and water vapor, $\overline{f_T f_q}$. Figure 7 shows saturation ratio PDFs for several values of $\overline{f_T f_q}$ in Fig. 7a, and the corresponding mixing diagrams in Fig. 7b. The temperature difference is chosen to be 8 K (corresponding to Fig. 9 from Chandrakar et al. 2020a), so that for cloud-free RBC with saturated boundary conditions any point in the bulk of the chamber cannot be subsaturated. However, by varying the correlation coefficient of $\overline{f_T f_q}$, such non-physical subsaturation fluctuations can be seen to exist. For an 8-K temperature difference, correlation coefficients of

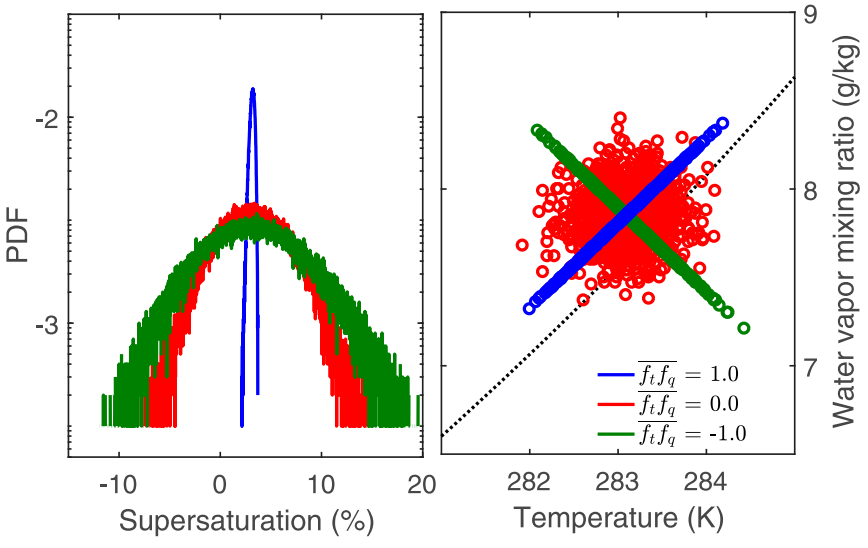

FIG. 5. (a) The saturation ratio PDF and (b) the mixing ratio vs temperature for different correlation coefficients ($\overline{f_T f_q}$) shown in different colors. Results are plotted assuming equal scalar diffusivities with $\Delta T = 8$ K. The mean temperature and the variance of scalars are the same across the different cases.

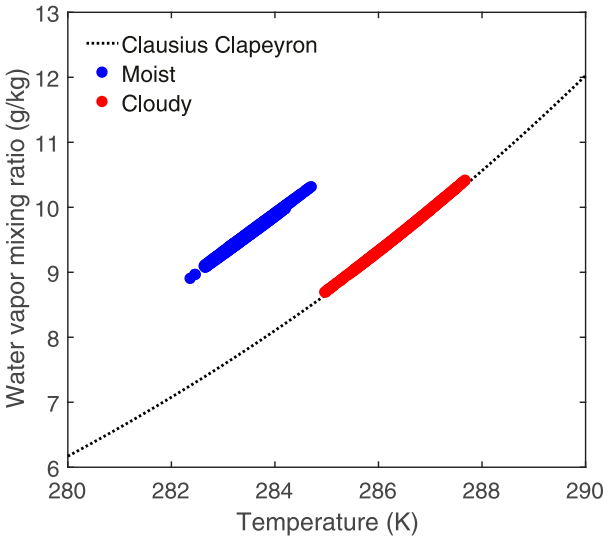

FIG. 6. Mixing ratio vs temperature for cloud-free (blue) and cloudy (red) conditions simulated using LES for $\Delta T = 20$ K with $T_m = 283.16$ K, with equal diffusivities for temperature and water vapor. On reaching a steady-state cloudy condition, the water vapor mixing ratio moves closer to the Clausius–Clapeyron line.

0.5 (green), 0.0 (purple), and −0.5 (black) are cases identical to those specified in Paoli and Shariff (2009); with supersaturation fluctuations induced by water vapor alone (red) as in Saito et al. (2019); and with correlation coefficient of 1.0 (blue) from cloud-free one-dimensional turbulence model (ODT) as in Chandrakar et al. (2020a).

It should be noted that even though cloud-free RBC requires the forcings of temperature and water vapor to follow a relation of the form $\sigma_T \sim \sigma_{q_v} \Delta T/\Delta q_v$, that is not necessarily the case in all atmospheric contexts. For example, in the case of cloud-top entrainment (Mellado 2017), even though entrained air from above a capping inversion is at higher temperature, it is drier than the cloud air itself. Forcing terms for the air from a capping inversion region would have a correlation coefficient closer to −1, resulting in a more symmetric PDF for supersaturation fluctuations. In contrast, for lateral entrainment from subsiding shells into a cumulus cloud, the temperature and water vapor is more likely to be positively correlated (Katzwinkel et al. 2014).

For LES studies of the convection-cloud chamber (Chang et al. 2016) such as in Thomas et al. (2019), the boundary fluxes are modeled using Monin–Obukhov similarity theory, resulting in a perfectly correlated forcing from the boundaries. However, in the subgrid-scale model the temperature and water vapor fields are diffused with the same turbulent diffusivity. Therefore, any positive supersaturations arising due to differential diffusivity are not captured, thus impeding the cloud droplet growth. Therefore, the droplet size distributions obtained from such simulations should be at least somewhat narrower than what would arise from experiments or from a DNS accounting for differential diffusivity. In DNS studies that do not account for differential diffusivity effects, such as the cloud parcel studies by Saito et al. (2019) that have only water vapor forcing (refer to the red points in Fig. 7), a broader

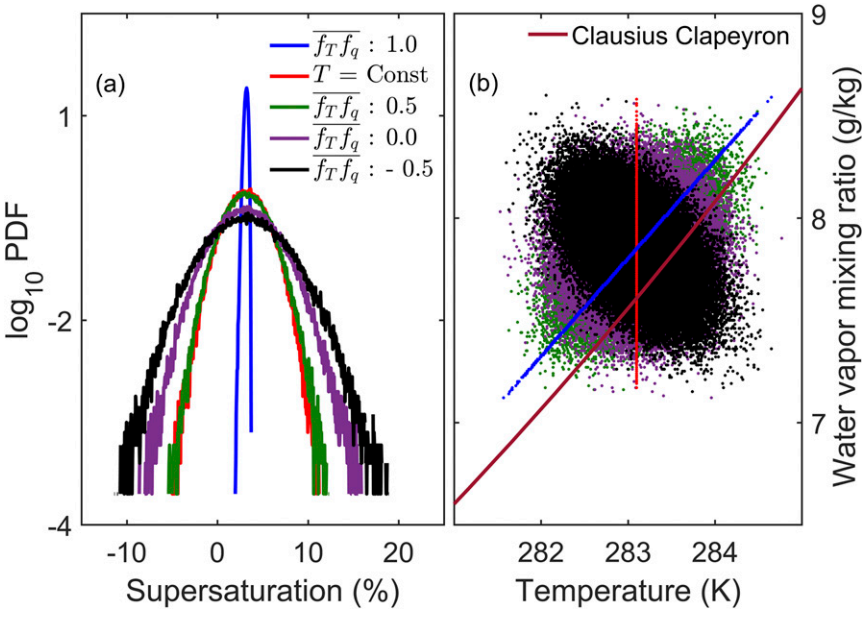

FIG. 7. (a) Saturation ratio PDF and (b) mixing ratio for different correlation coefficients ($\overline{f_T f_q}$) from studies by Paoli and Shariff (2009), Saito et al. (2019), and Chandrakar et al. (2020a) shown in different colors. Results are plotted assuming same scalar diffusivities with $\Delta T = 8$ K. This temperature difference is chosen to match the supersaturation PDF shown in Fig. 9 of Chandrakar et al. (2020a). Supersaturation fluctuations introduced by keeping temperature constant and fluctuating water vapor mixing ratio (red) (Saito et al. 2019).

size distribution of cloud droplets is obtained than warranted by a physically consistent supersaturation field.

Atmospheric models (Clark 1973; Khairoutdinov and Randall 2003) typically use two separate prognostic variables to capture temperature and water vapor. Subsequently, the diagnostic variable—mean supersaturation—is calculated from temperature and water vapor in individual grid boxes ignoring any subgrid-scale variability that is important for cloud droplet activation (Prabhakaran et al. 2020) and growth (Chandrakar et al. 2016). The calculated supersaturation interacts with the microphysics scheme to produce cloud droplet numbers and the corresponding masses or higher moments depending on the scheme's complexity. Often, DNS studies (Siewert et al. 2017; Sardina et al. 2018; Li et al. 2018) intended to understand the cloud droplet growth in a turbulent environment and treat supersaturation as a prognostic scalar disregarding the nonlinear behavior of the Clausius–Clapeyron equation. The treatment of supersaturation as a scalar is suitable in regimes where the Clausius–Clapeyron equation can be linearly approximated. However, in systems such as Rayleigh–Bénard convection, this is no longer true since the production of mixing supersaturation relies inherently on the nonlinear behavior of the Clausius–Clapeyron equation. Furthermore, there may be scenarios in which differential diffusivity needs to be accounted for, which would lead to the decorrelation of $\overline{q_v' T'}$. Ignoring such processes may result in overestimating the effect of turbulence on droplet growth. Finally, the correlation between temperature and water vapor depends on the processes that produce these fluxes. Hence, careful evaluation of the correlation of temperature and water vapor is needed to accurately capture the extend of supersaturation fluctuations, as demonstrated earlier.

In the larger context, the concerns about subgrid-scale variability of temperature, water vapor and subsequent microphysics interactions highlighted by Sommeria and Deardorff (1977) and Clark (1973) remains an open challenge even today, even in spite of LES studies with increasing resolution. One approach for addressing the subgrid-scale fluctuations considered by Hoffmann et al. (2019) is the use of a linear-eddy model, although this may be computationally expensive in full implementation. However, the GMM described here may provide a computationally inexpensive but efficient alternative to incorporate physically consistent subgrid-scale variability. A second part of the puzzle, involving supersaturation–cloud particle interactions still needs to be addressed. Reexamination of lateral entrainment studies with the consideration of negatively skewed supersaturation–microphysics interactions in the context of droplet activation and growth can help in answering the latter part of the puzzle.

Acknowledgments. This work was supported by National Science Foundation Grant AGS-1754244. We thank the two anonymous reviewers, Dr. Susan C. van den Heever, Dr. Mikhail Ovchinnikov, and Dr. Fan Yang for suggestions that improved the manuscript. Portage, a high-performance computing infrastructure at Michigan Technological University, was used in obtaining results presented in this publication. The data are permanently archived at MTU Digital Commons, https://digitalcommons.mtu.edu/all-datasets/4/.

APPENDIX

List of Symbols

q_v	Water vapor mixing ratio
$q_{\text{sat}}(T)$	Saturation vapor mixing ratio at temperature T
$q_v/q_{\text{sat}}(T)$	Saturation ratio
$\mathbf{U}$	Velocity vector of the fluid
$\dot{q}_l$	Rate of condensation/evaporation of water vapor
L_v	Latent heat of vaporization of water
C_p	Specific heat of air at constant pressure
f_T, f_q	External forces on T and q_v
$\rho_{t/b}$	Density of air at top (t) and bottom (b)
$T_{t/b}$	Temperature at top (t) and bottom (b)
$q_{vt/b}$	Water vapor mixing ratio at top (t) and bottom (b)
ν_v	Water vapor diffusivity
α	Thermal diffusivity
Le	Lewis number (α/ν_v)
ΔT	Temperature difference between top and bottom plate
Δq_v	Water vapor mixing ratio difference between top and bottom plate
σ_T	Standard deviation of temperature T
σ_{q_v}	Standard deviation of water vapor mixing ratio q_v
Sc	Schmidt number (ν/ν_v)
Pr	Prandtl number (ν/α)
Le	Lewis number (α/ν_v)
ν	Momentum diffusivity
ν_v	Water vapor diffusivity
α	Thermal diffusivity
C_1	Proportionality constant for Eqs. (16) and (17)
z	Vertical location in the chamber, assumed to be $0.5H$
H	Height of the chamber
Ra_m	Moist Rayleigh number $\left(\frac{g\beta\Delta T H^3}{\nu\alpha} + \frac{g\varepsilon\Delta q_v H^3}{\nu\alpha}\right)$
g	Acceleration due to gravity
β	Thermal expansion coefficient ($1/\overline{T}$)
ε	Ratio of gas constants of air and water vapor ($\approx$0.622)

REFERENCES

Abade, G. C., W. W. Grabowski, and H. Pawlowska, 2018: Broadening of cloud droplet spectra through eddy hopping: Turbulent entraining parcel simulations. *J. Atmos. Sci.*, **75**, 3365–3379, https://doi.org/10.1175/JAS-D-18-0078.1.

Capek, T., J. Borysow, C. Mazzoleni, and M. Moraldi, 2020: Toward non-invasive measurement of atmospheric temperature using vibro-rotational Raman spectra of diatomic gases. *Remote Sens.*, **12**, 4129, https://doi.org/10.3390/rs12244129.

Chandrakar, K. K., W. Cantrell, K. Chang, D. Ciochetto, D. Niedermeier, M. Ovchinnikov, R. A. Shaw, and F. Yang, 2016: Aerosol indirect effect from turbulence-induced broadening of cloud-droplet size distributions. *Proc. Natl. Acad. Sci. USA*, **113**, 14 243–14 248, https://doi.org/10.1073/pnas.1612686113.

——, ——, and R. A. Shaw, 2018: Influence of turbulent fluctuations on cloud droplet size dispersion and aerosol indirect

effects. *J. Atmos. Sci.*, **75**, 3191–3209, https://doi.org/10.1175/JAS-D-18-0006.1.

——, ——, S. Krueger, R. A. Shaw, and S. Wunsch, 2020a: Supersaturation fluctuations in moist turbulent Rayleigh–Bénard convection: A two-scalar transport problem. *J. Fluid Mech.*, **884**, A19, https://doi.org/10.1017/jfm.2019.895.

——, I. Saito, F. Yang, W. Cantrell, T. Gotoh, and R. A. Shaw, 2020b: Droplet size distributions in turbulent clouds: Experimental evaluation of theoretical distributions. *Quart. J. Roy. Meteor. Soc.*, **146**, 483–504, https://doi.org/10.1002/qj.3692.

Chang, K., and Coauthors, 2016: A laboratory facility to study gas–aerosol–cloud interactions in a turbulent environment: The π chamber. *Bull. Amer. Meteor. Soc.*, **97**, 2343–2358, https://doi.org/10.1175/BAMS-D-15-00203.1.

Clark, T. L., 1973: Numerical modeling of the dynamics and microphysics of warm cumulus convection. *J. Atmos. Sci.*, **30**, 857–878, https://doi.org/10.1175/1520-0469(1973)030<0857:NMOTDA>2.0.CO;2.

Cooper, W. A., 1989: Effects of variable droplet growth histories on droplet size distributions. Part I: Theory. *J. Atmos. Sci.*, **46**, 1301–1311, https://doi.org/10.1175/1520-0469(1989)046<1301:EOVDGH>2.0.CO;2.

Ditas, F., R. Shaw, H. Siebert, M. Simmel, B. Wehner, A. Wiedensohler, and M. Krämer, 2012: Aerosols-cloud microphysics-thermodynamics-turbulence: Evaluating supersaturation in a marine stratocumulus cloud. *Atmos. Chem. Phys.*, **12**, 2459–2468, https://doi.org/10.5194/acp-12-2459-2012.

Fan, J., M. Ovtchinnikov, J. M. Comstock, S. A. McFarlane, and A. Khain, 2009: Ice formation in Arctic mixed-phase clouds: Insights from a 3-D cloud-resolving model with size-resolved aerosol and cloud microphysics. *J. Geophys. Res.*, **114**, D04205, https://doi.org/10.1029/2008JD010782.

Gerber, H., 1991: Supersaturation and droplet spectral evolution in fog. *J. Atmos. Sci.*, **48**, 2569–2588, https://doi.org/10.1175/1520-0469(1991)048<2569:SADSEI>2.0.CO;2.

Hoffmann, F., T. Yamaguchi, and G. Feingold, 2019: Inhomogeneous mixing in Lagrangian cloud models: Effects on the production of precipitation embryos. *J. Atmos. Sci.*, **76**, 113–133, https://doi.org/10.1175/JAS-D-18-0087.1.

Katzwinkel, J., H. Siebert, T. Heus, and R. A. Shaw, 2014: Measurements of turbulent mixing and subsiding shells in trade wind cumuli. *J. Atmos. Sci.*, **71**, 2810–2822, https://doi.org/10.1175/JAS-D-13-0222.1.

Khain, A., M. Ovtchinnikov, M. Pinsky, A. Pokrovsky, and H. Krugliak, 2000: Notes on the state-of-the-art numerical modeling of cloud microphysics. *Atmos. Res.*, **55**, 159–224, https://doi.org/10.1016/S0169-8095(00)00064-8.

Khairoutdinov, M. F., and D. A. Randall, 2003: Cloud resolving modeling of the ARM summer 1997 IOP: Model formulation, results, uncertainties, and sensitivities. *J. Atmos. Sci.*, **60**, 607–625, https://doi.org/10.1175/1520-0469(2003)060<0607:CRMOTA>2.0.CO;2.

Korolev, A. V., and G. A. Isaac, 2000: Drop growth due to high supersaturation caused by isobaric mixing. *J. Atmos. Sci.*, **57**, 1675–1685, https://doi.org/10.1175/1520-0469(2000)057<1675:DGDTHS>2.0.CO;2.

——, and I. P. Mazin, 2003: Supersaturation of water vapor in clouds. *J. Atmos. Sci.*, **60**, 2957–2974, https://doi.org/10.1175/1520-0469(2003)060<2957:SOWVIC>2.0.CO;2.

Kostinski, A., 2009: Simple approximations for condensational growth. *Environ. Res. Lett.*, **4**, 015005, http://doi.org/10.1088/1748-9326/4/1/015005.

Krueger, S. K., 2020: Equilibrium droplet size distributions in a turbulent cloud chamber with uniform supersaturation. *Atmos. Chem. Phys.*, **20**, 7895–7909, https://doi.org/10.5194/acp-20-7895-2020.

Kulmala, M., A. Laaksonen, R. J. Charlson, and P. Korhonen, 1997a: Clouds without supersaturation. *Nature*, **388**, 336–337, https://doi.org/10.1038/41000.

——, Ü. Rannik, E. L. Zapadinsky, and C. F. Clement, 1997b: The effect of saturation fluctuations on droplet growth. *J. Aerosol Sci.*, **28**, 1395–1409, https://doi.org/10.1016/S0021-8502(97)00015-3.

Li, X.-Y., G. Svensson, A. Brandenburg, and N. E. Haugen, 2018: Cloud-droplet growth due to supersaturation fluctuations in stratiform clouds. *Atmos. Chem. Phys.*, **19**, 639–648, https://doi.org/10.5194/acp-19-639-2019.

Mellado, J. P., 2017: Cloud-top entrainment in stratocumulus clouds. *Annu. Rev. Fluid Mech.*, **49**, 145–169, https://doi.org/10.1146/annurev-fluid-010816-060231.

Niemela, J., L. Skrbek, K. Sreenivasan, and R. Donnelly, 2000: Turbulent convection at very high Rayleigh numbers. *Nature*, **404**, 837–840, https://doi.org/10.1038/35009036.

Paoli, R., and K. Shariff, 2009: Turbulent condensation of droplets: Direct simulation and a stochastic model. *J. Atmos. Sci.*, **66**, 723–740, https://doi.org/10.1175/2008JAS2734.1.

Pinsky, M., and A. Khain, 2018: Theoretical analysis of the entrainment–mixing process at cloud boundaries. Part I: Droplet size distributions and humidity within the interface zone. *J. Atmos. Sci.*, **75**, 2049–2064, https://doi.org/10.1175/JAS-D-17-0308.1.

Prabhakaran, P., A. S. M. Shawon, G. Kinney, S. Thomas, W. Cantrell, and R. A. Shaw, 2020: The role of turbulent fluctuations in aerosol activation and cloud formation. *Proc. Natl. Acad. Sci. USA*, **117**, 16 831–16 838, https://doi.org/10.1073/pnas.2006426117.

Saito, I., T. Gotoh, and T. Watanabe, 2019: Broadening of cloud droplet size distributions by condensation in turbulence. *J. Meteor. Soc. Japan*, **97**, 867–891, https://doi.org/10.2151/jmsj.2019-049.

Sardina, G., S. Poulain, L. Brandt, and R. Caballero, 2018: Broadening of cloud droplet size spectra by stochastic condensation: Effects of mean updraft velocity and CCN activation. *J. Atmos. Sci.*, **75**, 451–467, https://doi.org/10.1175/JAS-D-17-0241.1.

Siebert, H., and R. A. Shaw, 2017: Supersaturation fluctuations during the early stage of cumulus formation. *J. Atmos. Sci.*, **74**, 975–988, https://doi.org/10.1175/JAS-D-16-0115.1.

Siewert, C., J. Bec, and G. Krstulovic, 2017: Statistical steady state in turbulent droplet condensation. *J. Fluid Mech.*, **810**, 254–280, https://doi.org/10.1017/jfm.2016.712.

Sommeria, G., and J. Deardorff, 1977: Subgrid-scale condensation in models of nonprecipitating clouds. *J. Atmos. Sci.*, **34**, 344–355, https://doi.org/10.1175/1520-0469(1977)034<0344:SSCIMO>2.0.CO;2.

Sreenivasan, K. R., 2019: Turbulent mixing: A perspective. *Proc. Natl. Acad. Sci. USA*, **116**, 18 175–18 183, https://doi.org/10.1073/pnas.1800463115.

Thomas, S., M. Ovchinnikov, F. Yang, D. van der Voort, W. Cantrell, S. K. Krueger, and R. A. Shaw, 2019: Scaling of an atmospheric model to simulate turbulence and cloud microphysics in the Pi chamber. *J. Adv. Model. Earth Syst.*, **11**, 1981–1994, https://doi.org/10.1029/2019MS001670.

Vaillancourt, P., M. Yau, P. Bartello, and W. W. Grabowski, 2002: Microscopic approach to cloud droplet growth by

condensation. Part II: Turbulence, clustering, and condensational growth. *J. Atmos. Sci.*, **59**, 3421–3435, https://doi.org/10.1175/1520-0469(2002)059<3421:MATCDG>2.0.CO;2.

Wyngaard, J. C., 2010: *Turbulence in the Atmosphere*. Cambridge University Press, 406 pp.

Yang, F., R. McGraw, E. P. Luke, D. Zhang, P. Kollias, and A. M. Vogelmann, 2019: A new approach to estimate supersaturation fluctuations in stratocumulus cloud using ground-based remote-sensing measurements. *Atmos. Meas. Tech.*, **12**, 5817–5828, https://doi.org/10.5194/amt-12-5817-2019.

Yau, M. K., and R. R. Rogers, 1996: *A Short Course in Cloud Physics*. Elsevier, 304 pp.

Zhang, L., K. L. Chong, and K.-Q. Xia, 2019: Moisture transfer by turbulent natural convection. *J. Fluid Mech.*, **874**, 1041–1056, https://doi.org/10.1017/jfm.2019.463.